

Improvement of Ghost Imaging-OCT High-Resolution Real-Time Imaging

Decai Huyan^a and Tatsuo Shiina^b

Graduate School of Science and Engineering, Chiba University, Chiba-shi, Japan

Keywords: OCT, Ghost Imaging, Machine Learning.

Abstract: We previously proposed a novel system composed of GI (ghost imaging) and OCT (optical coherence tomography) to solve the problem of scattering and absorption by OCT measuring within scattering media. It is named GI-OCT. And we successfully obtained images of scattering media and target separately in a $2 \times 2\text{mm}$. In this paper, we improve a new computational approach to deal with the significant computational demands arising from increased image resolution. Using DIP (deep image prior) technique, we obtained images with minimal measurement data compared to traditional computational methods. In the simulation, the number of measurements required to obtain a clear image was reduced to 10%.


1 INTRODUCTION


Optical Coherence Tomography (OCT) is an advanced imaging technique capable of generating high-resolution tomographic images through a non-contact, non-invasive approach in non-homogeneous mediums (Huang et al., 1991). Operating on the principle of low-coherence interference, OCT combines reflected light from measurement and reference paths to reconstruct the optical property distribution of an object in the depth direction. Widely employed in commercial applications, OCT has demonstrated remarkable success in ophthalmology, providing intricate images of the inner retina. Recently, its application has extended to cardiology and dermatology for diagnostic purposes (Gambichler et al., 2005; Sinclair et al., 2015; Schwartz et al., 2017; Spaide et al., 2018; Vabre et al., 2012). Furthermore, OCT finds utility in various biomedical scenarios, particularly in multilayer scattering media such as organs and skin (Kirillin et al., 2008). This imaging technique is crucial in early skin cancer detection and other biomedical applications.

In recent years, ghost imaging (GI) techniques have attracted attention for their ability to separate signals from noise. Since publishing "ghost imaging using a single detector (Bromberg et al., 2009)", GI has been used in many fields (Lindell and Wet-

zstein, 2020; Shapiro, 2008; Katkovnik and Astola, 2012; Ryczkowski et al., 2016; Devaux et al., 2016; Zhao et al., 2012; Chen and Chen, 2013; Olivieri et al., 2020; Miot et al., 2019). Researchers in this paper demonstrated that a single probe can illuminate a sample multiple times with different light patterns, and reconstruct an image based on the relationship between the reflected light total intensity and the illuminated light pattern.

We previously proposed a novel system consisting of GI and OCT to solve the scattering and absorption challenges encountered in OCT measurements in scattering media, named GI-OCT (Huyan et al., 2022). This challenge refers to the fact that during OCT measurements in scattering media, the target signal is always affected by light attenuation and scattering in the scattering media when the measured light propagates in the depth direction. The scattering media may change the direction of the measured light, causing a time delay. This makes it difficult to obtain the exact shape of the target and a proper image of the target in the scattering media. GI-OCT utilizes the ability of GI to reconstruct an image even when the signal-to-noise ratio is low due to scattering. Using GI-OCT, obtaining an image of the target without scattering effects is possible. We successfully obtained no scattering effects images of the target in a scattering media in the range of $2 \times 2\text{mm}$ (Huyan et al., 2023). In practical OCT applications, high resolution and quick calculation are required for precise and accurate results. However, in GI-OCT, a large

^a  <https://orcid.org/0000-0002-2490-0439>

^b  <https://orcid.org/0000-0001-9292-4523>

number of single-pixel measurements are required because each sample contains only a small amount of information about the object. Specifically, in the computational method, the result that best obtains an image of N pixels requires at least $M = N$ measurements to meet $\beta = M/N = 100\%$, where β represents the sampling rate. In our practical measurement situation, measurements of $M > 4N$ are required to obtain good-quality images. This leads to a positive correlation between the number of pixels of the object and the data acquisition time, which is almost impossible to accomplish for instantaneous high-resolution images. Therefore, an important and long-term goal of advancing GI-OCT is to reduce the value β while maintaining good resolution, thus reducing the burden of data acquisition and obtaining better imaging quality.

With the development of deep learning, more and more methods are being used to solve GI computations. For example, deep learning-based GI (GIDL)(Lyu et al., 2017) and Deep Image Prior (DIP)(Lempitsky et al., 2018). This GIDL technique uses a deep neural network (DNN) to learn from a large number of input-output data pairs in order to establish mapping relationships between them. However, the experiments require access to huge training sets, which is both time-consuming and laborious, and the trained models can only reconstruct objects similar to the training set well, and the generalization challenge is the major problem.

DIP uses an untrained neural network as a constraint for image processing tasks such as denoising, inpainting, and super-resolution. The generator network can be used without prior training, thus eliminating the need for tens of thousands of labeled data. At the same time, this technique is used for GI computation, Deep neural network Constraint (GIDC) (Wang et al., 2022), which inputs the differential ghost imaging (DGI) reconstruction results into a randomly initialized neural network (untrained) to reconstruct remarkably high signal-to-noise ratio GI images at very low sampling rates β .

Inspired by the GIDC concept, we install here the DIP technique for GI-OCT, where the GI-OCT reconstruction results are input into a randomly initialized neural network, and the results are computed by the DIP technique to obtain good images at a small number of measurements. This enables the GI-OCT technique to obtain high resolution while reducing the number of measurements accomplishing fast and high-resolution measurements of biological samples.

In this paper, we have accomplished the application of the DIP technique in a simulation to confirm the results for 64×64 at $\beta = 10\%$, obtaining a clear

image. The calculation of 64×64 at $\beta = 10\%$ and 25% was accomplished in experiments, and a better target image was obtained.

2 METHOD

2.1 Concept of GI-OCT

GI-OCT is the solution to the problem of scattering media. The target in the scattering media (scattering sample) is simplified into two parts in OCT measurements. The former part is the scatter layer before the light hits the target. The latter part is the target layer. By changing the reference path (A-scan) and moving the probe orthogonally (B-scan), conventional OCT can construct a 3-dimensional image of the target layer in the scattering sample, as shown in Figure 1. However, the measured intensity distribution from the target layer has been affected because the image always has some uneliminated effects from the former scattering layers. When OCT measures the optical properties (transmittance and absorbance) of the target layer, the former scattering layers' distribution may change the light direction, or delay the received signal of the target layer due to the scatterer's influence. As a result, the optical properties with the scattering effect of the target layer are detected.

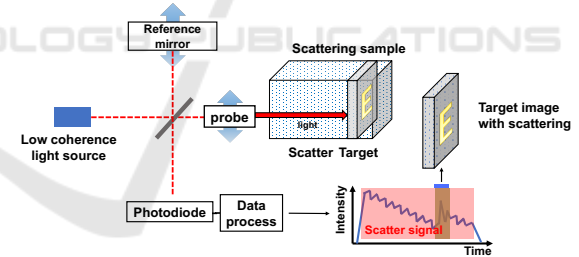


Figure 1: Setup of a conventional OCT, that produces the target image with scattering influence.

The GI-OCT concept is shown in Figure 2, where light passes through an expander and a spatial light modulator (SLM), and light patterns are generated to illuminate the target layer within the scattering sample. A single detector collects light intensity from the target and scatter layers. Each illuminated light pattern in GI-OCT produces an A-scan signal, which is a series of light intensities in the depth direction. With the OCT axial resolution, these series of light intensities can be separated as the summed intensity of each layer distribution. With the GI method, the correlation between the different light patterns and the summed intensity of each separated layer is calculated after repeated measurements using different light patterns.

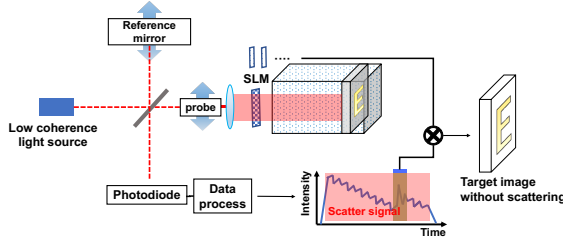


Figure 2: Setup of GI-OCT, that produces the scatter image that can be used to generate the target image without the scattering influence.

Instead of conventional OCT setups using a point measurement, GI-OCT uses a 2D measurement. This detector can simultaneously measure lights going in other directions or the signal delayed by scattering media. The results show them as scatter distributions. After this, we can compute the distribution of the target layer using the GI method and the distribution of the former scattering layer using the same method. The former scatter layer distribution can be used to correct the optical properties of the target layer.

2.2 The Calculation of GI-OCT

Figure 3 shows the schematic diagram of the GI-OCT method for detecting the distribution of sample layers.

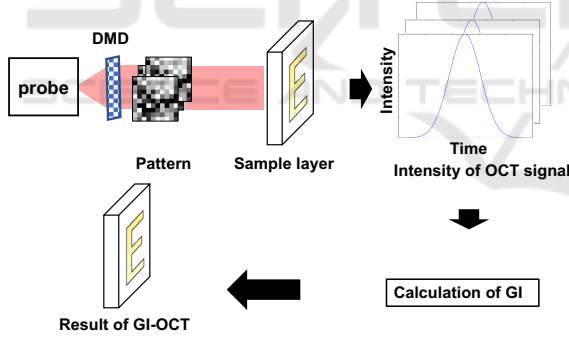


Figure 3: Setup of GI-OCT, that produces the scatter image that can be used to generate the target image without the scattering influence.

In order to obtain the OCT light intensity, different patterns of light from the digital micromirror device (DMD) chip illuminate the sample layer, as defined in Eq. (1),

$$I_n = \alpha_n \beta(\text{sample}) \quad (1)$$

where α_n is the light pattern with $m \times m$ speckles illuminated from the DMD chip; $\beta(\text{sample})$ is the transmittance distribution of the sample layer; I_n is the received light intensity summed from all speckles' intensities, which is the OCT interference light intensity. $\beta'(\text{sample})$ is the reconstructed image of the sample layer's transmittance distribution using the

computational ghost imaging (CGI) method by calculating the correlation between α_n and I_n as

$$\beta'(\text{sample})_{CGI} = \frac{1}{N} \sum_{n=1}^N (\alpha_n - \langle \alpha_n \rangle) I_n \quad (2)$$

where $\langle \alpha_n \rangle = \frac{1}{N} \sum_{n=1}^N \alpha_n$ is the average of light patterns.

The DGI is calculated using Eq. (3),

$$\begin{aligned} \beta'(\text{sample})_{DGI} &= \frac{1}{N} \sum_{n=1}^N (\alpha_n - \langle \alpha_n \rangle) (I_n - \frac{\langle I \rangle}{\langle I' \rangle} I'_n) \\ &= \frac{1}{N} \sum_{n=1}^N (\alpha_n - \langle \alpha_n \rangle) I_n^* \end{aligned} \quad (3)$$

where I'_n is the total light intensity of each light pattern without sample, and I_n^* is called the light transmission relative variance. Depending on the light transmission relative variance, DGI can have signal-to-noise ratios several orders of magnitude higher than CGI.

2.3 Faster Calculation

Because DGI requires a large amount of data, we use the GIDC technique in order to increase the computational speed and reduce the measurement time. GIDC provides the resulting DGI reconstruction into a randomly initialized neural network (untrained). After that, the output of the neural network is used as estimated values of the high-quality GI image. Finally, the weights of the neural network are updated to minimize the error between the measured and estimated values. As the error is minimized, the output of the neural network converges to a high-quality image. For the proposed GIDC, the function for reconstructing the object image is as Eq.(4) and (5).

$$\theta^* = \underset{\theta \in \Theta}{\text{argmin}} \|f_{\theta}(z) - \beta'(\text{sample})_{DGI}\|^2 \quad (4)$$

$$\beta'(\text{sample})_{GIDC} = f_{\theta^*}(z) \quad (5)$$

Where f is the neural network, Θ is the network parameter (obtained by random initialization at the beginning), z is a fixed random code initially inputted into the network, θ^* is the optimal solution of the parameter obtained by training, and $\beta'(\text{sample})_{GIDC}$ is the optimal output of the network, which is the reconstructed high-quality image. $\underset{\theta \in \Theta}{\text{argmin}}$ is the argument of the minimum, which makes the value of the variable when the formula obtains the minimum value.

Figure 4 shows the results obtained from the experiment using the original data from GIDC (data from GIDC)(Wang et al., 2022). Figure 4 shows the results of GIDC iterations on DGI reconstructed images. Figure 4 (a) shows the DGI results, in 64×64

size, computed 400 times. Figure 4 (b) results from training 0 times using the neural network. Figure 4 (c) and (d) are the results of iterations 100 and 200 times

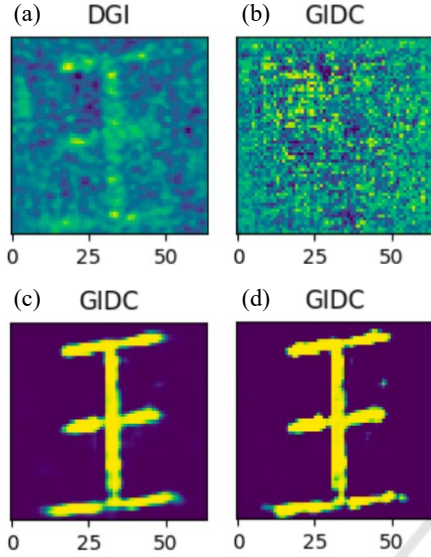


Figure 4: The results of (a) is DGI uses 64×64 to compute 400 times. (b), (c) and (d) are the results of training 0, 100 and 200 times.

3 SIMULATION

This simulation utilizes the GIDC network structure derived from the U-network. Algorithm 1 describes the main progress. The weights in the neural network are updated using an Adam optimizer with a learning rate $\alpha = 0.05$. The leakage parameter of Leaky ReLU is 0.2. The regularization parameter of TV is 10^{-10} . L refers to the number of iterations.

Data: DGI's result, $\alpha = 0.05$, Leaky ReLU=0.2, TV= 10^{-10} , L=400
Result: GI reconstruction with GIDC initialization: a randomly initialized parameters Θ in neural network (untrained).;
while Step=1,2,3... L **do**
 $f_{\theta}(z) = \theta \in \Theta$;
 $L_{\theta} = MSE(f_{\theta}(z) - \beta'(sample)_{DGI})$;
 $\theta = ADAM(L_{\theta}, \alpha)$
end

Algorithm 1: The algorithms of GIDC.

The sample used for the simulation is the character 'E', as shown in Figure 5.

Firstly, the corresponding light intensity (I) was obtained after illuminating the sample (β) with $64 \times$

64 size random pattern (α). Then, using the DGI calculation method of Eq. (3), the calculated result of the sample (β') was obtained by employing the pattern (α) and the light intensity (I). Finally, the calculated results were applied to the GIDC to obtain the results for 0, 100, and 200 iterations.

Figure 6 (a) shows the DGI results for character 'E' at 400 calculations with size 64×64 . Figure 6 (b) shows the result of 0 times training using neural network. Figure 6 (c) and (d) show the results for 100 and 200 iterations. We succeeded in getting clear images from only recognizable DGI images.

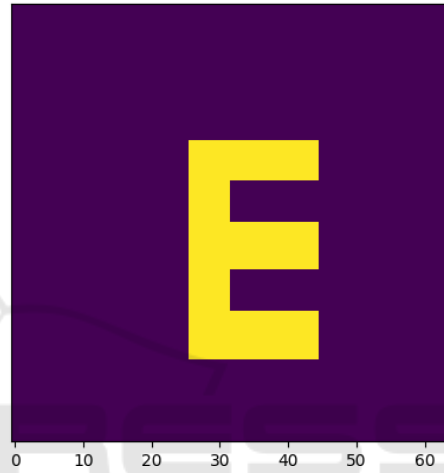


Figure 5: The character 'E' is utilized in the simulation.

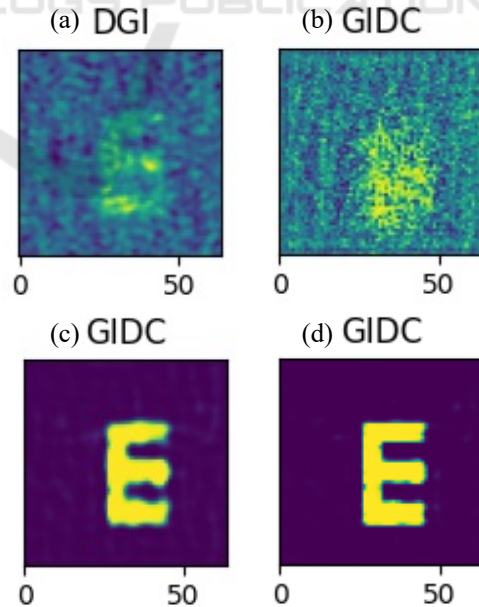


Figure 6: The results of (a) is DGI uses 64×64 to compute 400 times. (b), (c) and (d) are the results of training 0, 100 and 200 times.

4 EXPERIMENT AND SETUP

Figure 7 illustrates the experimental setup for GI-OCT.

In the GI-OCT, the axial resolution is equivalent to coherence length, defined as $\delta z = 0.44\lambda_0^2/\Delta\lambda$, where $\lambda_0 = 856\text{nm}$ is the central wavelength of a high-power Superluminescent diodes (SLD) light source with Gaussian distribution, and the equipment specifications are shown in Table 1.

Table 1: SLD specification of GI-OCT.

Manufacturer	THORLABS
Model number	SLD850S-A20W
Center wavelength	860 nm
Spectral band width	28 nm
Coherence length	11.6 μm
Optical power[MAX]	30 mW

To make illumination patterns, the GI-OCT beam must spread and reflect part of the light. In this study, a high-power SLD was prepared in order to validate the new GI-OCT algorithm. The reference path length scanning mechanism is composed of a steady rotating motor and a fixed mirror that completes the axial scanning process (Shiina et al., 2003). The measurement path is equipped with an optical probe, and a varifocal collimator makes a beam of 2 mm diameter. Meanwhile, the high-speed DMD chip is set in the measurement path, and its specifications are shown in Table 2.

Table 2: DMD specification of GI-OCT.

Manufacturer	TI
Model number	DLP2010LC
Illumination wavelength	860 nm (90%)
Array diagonal	5.29 mm
Output frame rate	240 Hz

On the DMD chip, micromirrors are arranged in a matrix of 854×480 , with a total size of $4.61 \times 2.59\text{mm}$. Each micromirror has a size of $5.4 \times 5.4\mu\text{m}$ and a deflection angle of ± 17 degrees on the diagonal axis, divided into two states, "on" and "off". In order to reflect pattern light back to the collimator, the DMD chip is tilted $+17$ degrees along the diagonal. The DMD chip was controlled to display a speckle pattern within a $1.5 \times 1\text{mm}^2$ DMD chip area, 64×64 were applied in this experiment.

The character "E" also shown on the DMD, which overlaps the illumination pattern, was used as the target object for this experiment to be able to focus on the reconstruction effect, as shown in Figure 5. In addition, the DMD chip was placed in the interference

region of the OCT so that the OCT measurements are efficient in terms of light reflection and stable in terms of light intensity, which makes it easy to reconstruct the results from the images.

In this paper, different number of measurements were prepared: 410 and 1000 measurements. In actual measurements, there will be a lot of noise and bias affecting the experimental results. It is not possible to get the $\beta=10\%$ in the simulation results and the number of measurements needs to be increased to enhance the results.

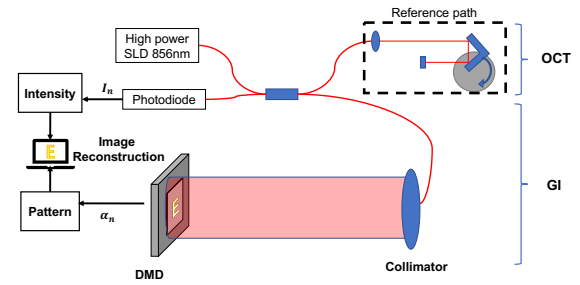


Figure 7: Experiment setup of GI-OCT.

5 RESULT

We have used the character 'E' of Figure 5 as the target image. Figure 8 shows the results at different numbers of iterations with the GIDC method and the DGI results, with the reconstructed image of the GI-OCT device at the actual number of measurements of 410, with a measurement pattern size of 64×64 . Figure 8 (a) shows the results of the DGI method. In this result, little information is obtained for each pattern, a large number of measurements are required to obtain a recognizable target image, and the reconstructed image has the shape of the target image. Figures 8(b), (c), (d), and (e) show the results for 0, 100, 200, 300, and 400 iterations. Among these results, the 0th result is the worst, which is consistent with the simulation result (Fig.6 (a)). However, from the 100th iteration, the iteration results hardly change anymore and the reconstructed image is hardly visible as the target image.

Figure 9 shows the results using the GIDC method at different numbers of iterations and the DGI results with the reconstructed image of the GI-OCT device at the actual number of measurements of 1000, with a measurement pattern size of 64×64 . Figure 9 (a) shows the results of the DGI method. This result is almost identical to the DGI result in Figure 8 (a). Figures 9 (b), (c), (d), and (e) show the 0th, 100th, 200th, 300th, and 400th iteration results. Among these results, the same 0th result is the worst. The character

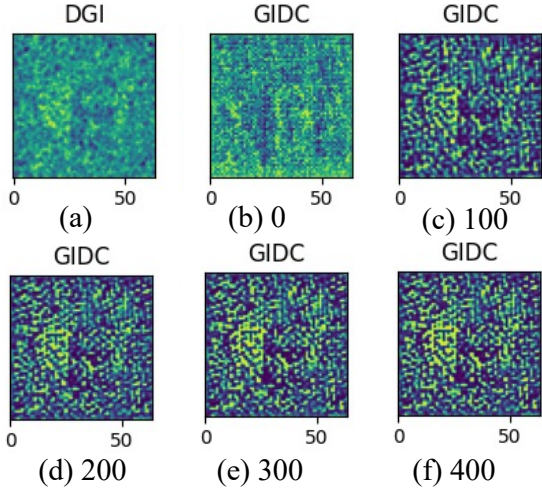


Figure 8: The results of each iteration by GIDC method and DGI method in 410 measurements.

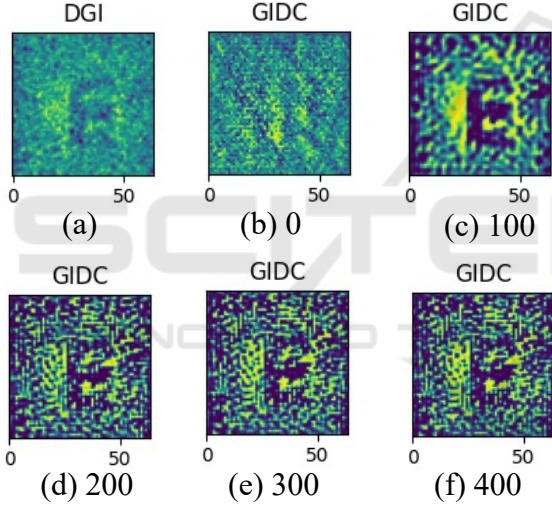


Figure 9: The results of each iteration by GIDC method and DGI method in 1000 measurements.

"E" is clearly visible in the 100th result image. After 200 times iterations, the iteration results progressively worsen, probably due to overfitting.

6 DISCUSSION

In this paper, the structural similarity index method (SSIM) is introduced for the purpose of evaluating the reconstructed images. SSIM is a method for predicting the perceived quality of two images. SSIM is close to 1, indicating that the perceived structure of the two images is consistent, while SSIM is close to 0, indicating that the images are unrelated. The SSIM results are used to make a subjective judgment of the

clarity of the image character "E", a positive SSIM value means that the reconstructed image is positively correlated and a negative value means that it is negatively correlated. The SSIM is used to evaluate the quality of the reconstructed image.

$$SSIM(x, y) = \frac{(2\mu_x\mu_y + (K_1L)^2)(2\sigma_{xy} + (K_2L)^2)}{(\mu_x^2 + \mu_y^2 + (K_1L)^2)(\sigma_x^2 + \sigma_y^2 + (K_2L)^2)} \quad (6)$$

here, x and y indicate the expected result and the comparison result. μ is the mean value, σ is the standard deviation, σ_{xy} is the covariance of x and y , $K_1 = 0.01$, $K_2 = 0.03$, and L represents the maximum possible pixel value in the image. The experimental images are compressed between 0 and 1; here, $L = 1$.

We compared the SSIM results for different number of measurements with different number of iterations.

By calculating the results of DGI and GIDC with the SSIM values of Figure 5, we obtain Figure 10. The SSIM of the DGI results for 410 measurements is 0.003. The SSIM of the GIDC with each 100 iterations, as shown by the blue line in Figure 10, reaches a maximum of 0.004 at 100 iterations, and the results are negative after 200 iterations. The SSIM of the DGI result for 1000 measurements was 0.005. The SSIM of the GIDC with every 100 iterations, as shown by the orange line in Figure 10, again reached a maximum of 0.006 at 100 iterations, after which they were all lower than 0.005 and did not change much. The above two experiments proved that using the GIDC method enhanced the image results at 100 iterations. The experimentally obtained SSIM has a very low value because the beam used in the actual measurement of GI-OCT has a Gaussian distribution. This resulted in a large difference between the GI-OCT image and the character 'E'. There is a lot of random noise, and it is impossible to achieve the good results obtained in the simulation using $\beta=10\%$. A higher number of measurements is needed.

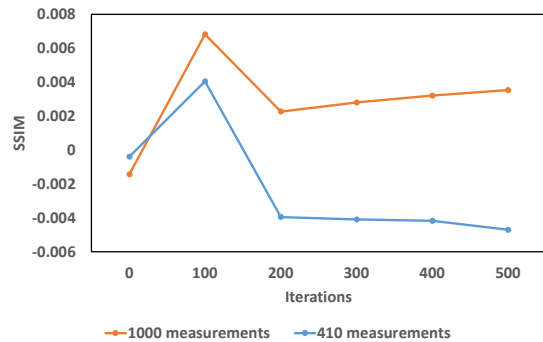


Figure 10: SSIM values of the GIDC results for different numbers of iterations for 410 and 1000 measurements.

7 CONCLUSION

In this study, we propose a new method applied to GI-OCT to reduce the number of measurements. We used the GIDC method, where the reconstruction results are added to a neural network, utilizing the fact that neural networks are inherently low resistance to natural signals and high resistance to noise.

We accomplished the reconstruction of GI-OCT images in simulation and obtained clear images at $\beta=10\%$, greatly reducing the number of measurements required for reconstruction in a size of 64×64 . It was experimentally verified that the method can enhance the reconstructed image at 100 iterations.

However, due to some problems, the SSIM values could be better. This result is due to the background light problem, which needs to be solved first in the future to get more correct results. It may also be due to the fact that different GI calculation methods can affect the imaging results. Therefore, it is necessary to compare the effects of different GI calculation methods on the reconstructed images, which are computed ghost imaging (CGI), pseudo-inverse ghost imaging (PGI), and differential pseudo-inverse ghost imaging (DPGI) (Don, 2019; Ferri et al., 2010; Zhang et al., 2014). In addition, the number of speckles in the GI-OCT illumination pattern can also greatly impact the results and is an issue we need to research in the future.

In the next step, we are going to apply this new technique to obtain real-time, high-resolution images of multilayers in scattering media of GI-OCT measurements.

REFERENCES

- Bromberg, Y., Katz, O., and Silberberg, Y. (2009). Ghost imaging with a single detector. *Physical Review A - Atomic, Molecular, and Optical Physics*, 79(5):1–4.
- Chen, W. and Chen, X. (2013). Ghost imaging for three-dimensional optical security. *Applied Physics Letters*, 103(22):1–5.
- Devaux, F., Moreau, P.-A., Denis, S., and Lantz, E. (2016). Computational temporal ghost imaging. *Optica*, 3(7):698.
- Don, M. (2019). *An Introduction to Computational Ghost Imaging with Example Code*.
- Ferri, F., Magatti, D., Lugiato, L. A., and Gatti, A. (2010). Differential ghost imaging. *Physical Review Letters*, 104(25):1–4.
- Gambichler, T., Moussa, G., Sand, M., Sand, D., Altmeyer, P., and Hoffmann, K. (2005). Applications of optical coherence tomography in dermatology. *Journal of Dermatological Science*, 40(2):85–94.
- Huang, D., Swanson, E. A., Lin, C. P., Schuman, J. S., Stinson, W. G., Chang, W., Hee, M. R., Flotte, T., Gregory, K., Puliafito, C. A., and Fujimoto, J. G. (1991). Optical coherence tomography. *Science*, 254(5035):1178–1181.
- Huyan, D., Lagrosas, N., and Shiina, T. (2022). Target imaging in scattering media using ghost imaging optical coherence tomography. *APL Photonics*, 7(8).
- Huyan, D., Lagrosas, N., and Shiina, T. (2023). Optical properties analysis of scattering media based on gi-oct imaging. *Photonics*, 10(2).
- Katkovnik, V. and Astola, J. (2012). Compressive sensing computational ghost imaging. *Journal of the Optical Society of America A*, 29(8):1556.
- Kirillin, M. Y., Priezzhev, A. V., and Myllylä, R. (2008). Role of multiple scattering in formation of OCT skin images. *Quantum Electronics*, 38(6):570–575.
- Lempitsky, V., Vedaldi, A., and Ulyanov, D. (2018). Deep Image Prior. *2018 IEEE/CVF Conference on Computer Vision and Pattern Recognition*, 128(7):9446–9454.
- Lindell, D. B. and Wetzstein, G. (2020). Three-dimensional imaging through scattering media based on confocal diffuse tomography. *Nature Communications*, 11(1):1–8.
- Lyu, M., Wang, W., Wang, H., Wang, H., Li, G., Chen, N., and Situ, G. (2017). Deep-learning-based ghost imaging. *Scientific Reports*, 7(1):1–6.
- Miot, C. A. G. A., Yczkowski, P. I. R., Riberg, A. R. I. T. F., Udley, J. O. H. N. M. D., and Enty, G. O. G. (2019). Ghost optical coherence tomography. *Optics*, 27(17):24114–24122.
- Olivieri, L., Gongora, J. S. T., Peters, L., Cecconi, V., Cutrona, A., Tunesi, J., Tucker, R., Pasquazi, A., and Peccianti, M. (2020). Hyperspectral terahertz microscopy via nonlinear ghost imaging. *Optica*, 7(2):186.
- Ryczkowski, P., Barbier, M., Friberg, A. T., Dudley, J. M., and Genty, G. (2016). Ghost imaging in the time domain. *Nature Photonics*, 10(3):167–170.
- Schwartz, M., Levine, A., and Markowitz, O. (2017). Optical coherence tomography in dermatology. *Cutis*, 100(3):163–166.
- Shapiro, J. H. (2008). Computational ghost imaging. *Physical Review A - Atomic, Molecular, and Optical Physics*, 78(6):1–4.
- Shiina, T., Moritani, Y., Ito, M., and Okamura, Y. (2003). Long-optical-path scanning mechanism for optical coherence tomography. *Applied Optics*, 42(19):3795.
- Sinclair, H., Bourantas, C., Bagnall, A., Mintz, G. S., and Kunadian, V. (2015). OCT for the identification of vulnerable plaque in acute coronary syndrome. *JACC: Cardiovascular Imaging*, 8(2):198–209.
- Spaide, R. F., Fujimoto, J. G., Waheed, N. K., Sadda, S. R., and Staurengi, G. (2018). Optical coherence tomography angiography. *Progress in Retinal and Eye Research*, 64(June 2017):1–55.
- Vabre, L., Dubois, A., Boccara, C., Vabre, L., Dubois, A., Boccara, C., Vabre, L., Dubois, A., and Boccara, A. C.

(2012). Thermal-light full-field optical coherence tomography.

Wang, F., Wang, C., Chen, M., Gong, W., Zhang, Y., Han, S., and Situ, G. (2022). Far-field super-resolution ghost imaging with a deep neural network constraint. *Light: Science and Applications*, 11(1):1–11.

Zhang, C., Guo, S., Cao, J., Guan, J., and Gao, F. (2014). Object reconstitution using pseudo-inverse for ghost imaging. *Optics Express*, 22(24):30063.

Zhao, C., Gong, W., Chen, M., Li, E., Wang, H., Xu, W., and Han, S. (2012). Ghost imaging lidar via sparsity constraints. *Applied Physics Letters*, 101(14):1–4.

